catalysts

MDPI

Article

Electrocatalytic Glucose Oxidation at Coral-Like Pd/C_3N_4-C Nanocomposites in Alkaline Media

Guang Dong [1,2], Qingqing Lu [1], Haihui Jiang [1], Chunfang Li [2], Yingying Gong [1], Haoquan Zhang [1] and Wenpeng Li [1,2,*]

1 Engineering & Technology Center of Electrochemistry, School of Chemistry and Pharmaceutical Engineering, Qilu University of Technology (Shandong Academy of Sciences), Jinan 250353, China; Duang3176@163.com (G.D.); qqlu@qlu.edu.cn (Q.L.); jhh@qlu.edu.cn (H.J.); gongyingying1124@163.com (Y.G.); haoquanzhang98@163.com (H.Z.)

2 Shandong Key Laboratory of Biochemical Analysis, College of Chemistry and Molecular Engineering, Qingdao University of Science and Technology, Qingdao 266042, China; lichunfang@qust.edu.cn

* Correspondence: liwenpeng@qlu.edu.cn or wenpengli75@163.com; Tel.: +86-531-8963-1208

Received: 23 March 2020; Accepted: 16 April 2020; Published: 19 April 2020

Abstract: Porous coral-like Pd/C_3N_4-C nanocomposites are fabricated by a simple one-pot chemical reduction method. Their electrocatalytic performance is ~50% higher than a carbon-loaded palladium electrocatalyst (Pd/C) in alkaline media. This confirms that the glucose electrooxidation and sensing performance of a Pd/C can be improved by the synergy of graphitic carbon nitride (C_3N_4), though C_3N_4 exhibits poor electrical conductivity. Compared to Pd/C, the size of Pd nanoparticles in Pd/C_3N_4-C decreases. As a result, the activity of Pd/C_3N_4-C is enhanced due to the higher dispersion and the synergistic effect. Pd/C_3N_4-C presents a rapid response and high sensitivity to glucose. The sensitivity for glucose sensing at Pd/C_3N_4-C is 3.3 times that of at Pd/C in the range of 0.001–10 mM. In the lower range of 0.001–1 mM, the sensitivity at Pd/C_3N_4-C is ~10 times greater than Pd/C.

Keywords: palladium; nitrogen carbide; electrocatalysts; glucose electrooxidation; nonenzymatic-glucose sensor

1. Introduction

Glucose electrooxidation reaction (GOR), which has been studied for more than 100 years [1], is the key chemical reaction in nonenzymatic-glucose sensors and direct glucose fuel cells [2,3]. Theoretically, glucose can be completely oxidized to CO_2 and H_2O, releasing 24 electrons:

$$C_6H_{12}O_6 + 24OH^- \rightarrow 6CO_2 + 18H_2O + 24e^- \quad (1)$$

however, to date, the complete electrooxidation of glucose is rarely reported. The main product for GOR is gluconate, and only two electrons are released [4]:

$$C_6H_{12}O_6 + 2OH^- \rightarrow C_6H_{12}O_7 + H_2O + 2e^- \quad (2)$$

In recent years, Pd and Pd compounds have been regarded as state of the art electrocatalytic active components for GOR [3,5–8]. Many efforts have been made to improve the activity of palladium-based catalysts. The activity of a catalyst depends not only on its active component but also on its support. It is an effective way to develop novel support to improve the activity of catalysts. A graphitic carbon nitride (C_3N_4) has a planar two-dimensional (2D) structure, and its surface is rich in nitrogen atoms with a strong coordination ability. We consider that C_3N_4 may be used as excellent electrocatalytic support in Pd-based catalysts for GOR. The Schottky effect [9] of C_3N_4-Pd facilitates electron migration

from metal to the N-type semiconductor C_3N_4 and benefits the electrooxidation reaction at Pd. In this work, porous coral-like Pd/C_3N_4-C nanocomposites were fabricated with the hydrogen bubbles as dynamic templates. GOR on Pd/C_3N_4-C was evaluated by electrochemical measurements in alkaline media. The electrocatalytic performance of Pd/C_3N_4-C is ~50% higher than Pd/C. Besides the activity for GOR, the Pd/C_3N_4-C shows competitive glucose-sensing performance compared to some other electrocatalysts reported recently [10–18] (Table 1). This confirms that Pd/C_3N_4-C is indeed a good electrocatalyst for GOR.

Table 1. Comparison of glucose oxidation on the Pd/C_3N_4-C electrode and other Pd electrodes.

Electrode	Applied Potential (vs. Hg/HgO)	Linear Range (mM)	LOD (μM)	Reference
Pd@Pt CINP/C/GCE [1]	+0.01 V	1–8.5	0.82	[10]
Pd-Ni-P	+0.65 V	0.005–10.24	0.15	[11]
Pd nanocubes	+0.50 V	1–10	N/A	[12]
WO_3-Pd AA [2]	+0.45 V	5–55, 65–375	N/A N/A	[13]
Pd-Fe/Ti	+0.13 V	0.002–3.0	1.0	[14]
Pd-CuO/rGO/SPE [3]	+0.70 V	0.006–22	0.03	[15]
Pt-Pd nanowire arrays	+0.30 V	Up to 10	N/A	[16]
Pd-Au cluster	+0.04 V	0.1–30	50	[17]
RGO-Pd NCs@CuO [4]	+0.50 V	0.001–3.1	0.01	[18]
Pd/C_3N_4-C	+0.50 V	0.1–10	0.55	This work

[1] CINP: core/island nanoparticles; GCE: glassy carbon electrode. [2] AA: after annealing. [3] SPE: screen printed electrodes. [4] NCs: nanocrystals.

2. Results

2.1. Physical Characterization

As can be seen from the images (Figure 1a–c) of the scanning electron microscope (SEM), Pd/C_3N_4-C possesses a porous coral-like structure. The mapping analysis in Figure 1d confirms the coexistence of elements Pd, C, and N in the catalyst. The spherical Vulcan carbon and the planar graphic nitrogen carbide are easy to assemble into three-dimensional (3D) structures. The hydrogen bubbles produced in the hydrolysis of $NaBH_4$ act as dynamic templates of the coral-like Pd/C_3N_4-C.

Pd particle sizes are estimated from images (Figure 2a–c) by transmission electron microscopy (TEM). All nanoparticles (NPs) in the images are considered. The average Pd particle sizes (Figure 2d–g) of Pd/C_3N_4, Pd/C, and Pd/C_3N_4-C are 3.6, 4.6, and 3.3 nm, respectively. The introduction of C_3N_4 dramatically decreases the diameter of palladium nanoparticles; thus, the total surface area is increased. More active sites can be provided with an increased surface. The N atoms in C_3N_4 exhibit a strong complexing ability for Pd atoms/ions [19], which is beneficial for strong metal support interactions. There are typical lattice fringes with 0.14, 0.19, and 0.23 nm, which are according to the (220), (200), and (111) planes (Figure 2g) of Pd nanocrystals, respectively. Some Pd NPs are bridging the C_3N_4 and carbon (Figure 2h), then C_3N_4-Pd-C heterostructures appear in Pd/C_3N_4-C composites.

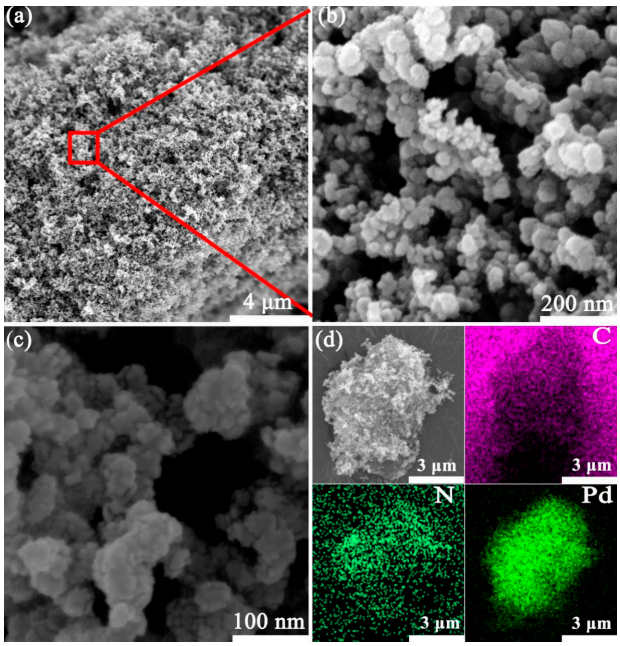

Figure 1. SEM (**a**–**c**) and element mapping images (**d**) of Pd/C_3N_4-C.

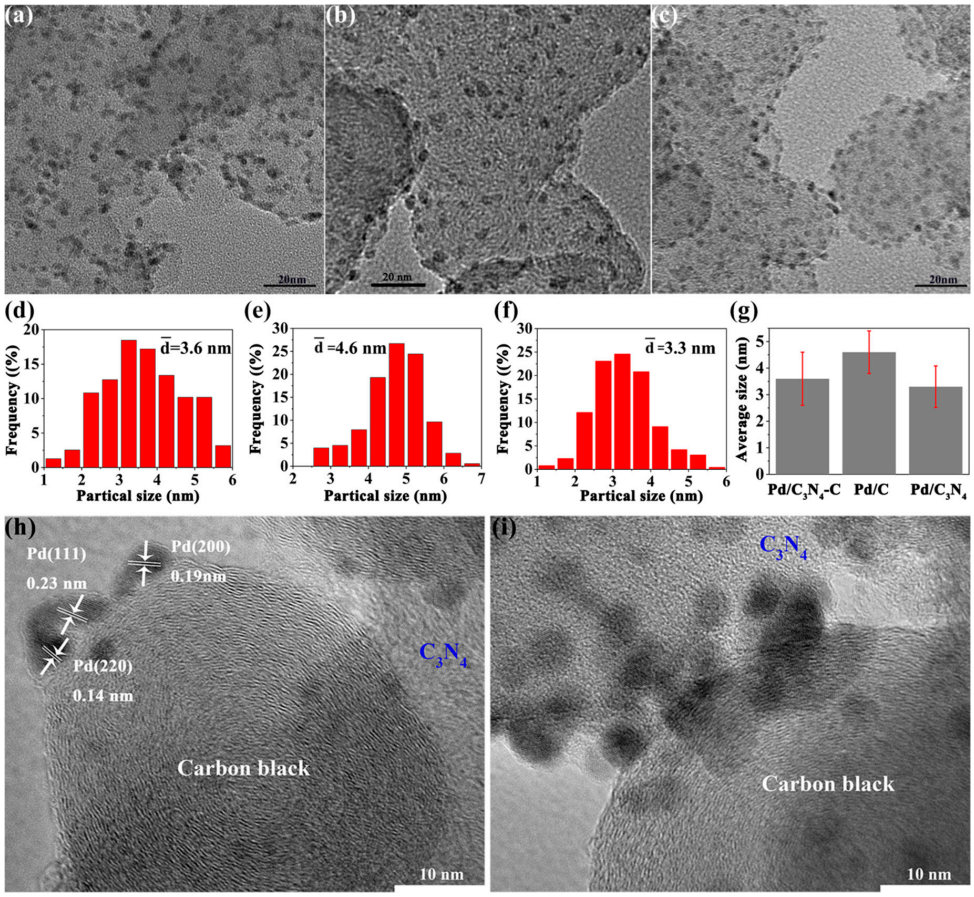

Figure 2. TEM images and corresponding histograms of Pd NPs size distribution. (**a**,**d**) Pd/C_3N_4, (**b**,**e**) Pd/C, and (**c**,**f**) Pd/C_3N_4-C. (**g**) The standard deviation of the Pd NPs sizes. (**h**,**i**) High-resolution TEM images of Pd/C_3N_4-C.

The X-ray diffraction(XRD) patterns of Pd/C_3N_4, Pd/C, and Pd/C_3N_4-C are shown in Figure 3a. The peak values at about 27° can be ascribed to the (002) interlayer stacking of C_3N_4. The peak values

at 39.7°, 45.6°, 67.7°, and 80.5° correspond to the Pd (111), (200), (220), and Pd (311) crystal faces, respectively. The peaks corresponding to the C (002) and C_3N_4 (002) crystal planes are significantly weakened in Pd/C_3N_4-C, compared with the C (002) peak of Pd/C and the C_3N_4 (002) peak of Pd/C_3N_4. It suggests that the assemble of C_3N_4 and carbon may mainly occur at the (002) crystal plane of C_3N_4 and the (002) crystal plane of Vulcan carbon. Similar changes of C_3N_4 (002) peak caused by facet coupling can also be found in other reports [20]. The lattice constants (α) and the size of Pd NPs (d) are calculated using Equation (3) [21,22] and the Scherrer's equation (Equation (4)) [23–26], respectively,

$$\alpha = \frac{\sqrt{2}\lambda}{\sin\theta_{max}} \quad (3)$$

$$d = \frac{\kappa\lambda}{\beta\cos\theta} \quad (4)$$

where λ is the wavelength of X-ray, θmax is the peak position of Pd (220), k is a numerical factor, and β is the width in radians (full-width at half-maximum) of the peak. θ is the Bragg angle. The lattice constants of Pd in Pd/C_3N_4-C and Pd/C are 0.3991 nm and 0.3977 nm, respectively. The average Pd NPs sizes in Pd/C_3N_4-C and Pd/C are 3.1 nm and 4.7 nm, respectively. The sizes estimated with XRD patterns are similar to the diameters of Pd/C_3N_4-C (3.3 nm) and Pd/C (4.6 nm) obtained from the TEM images.

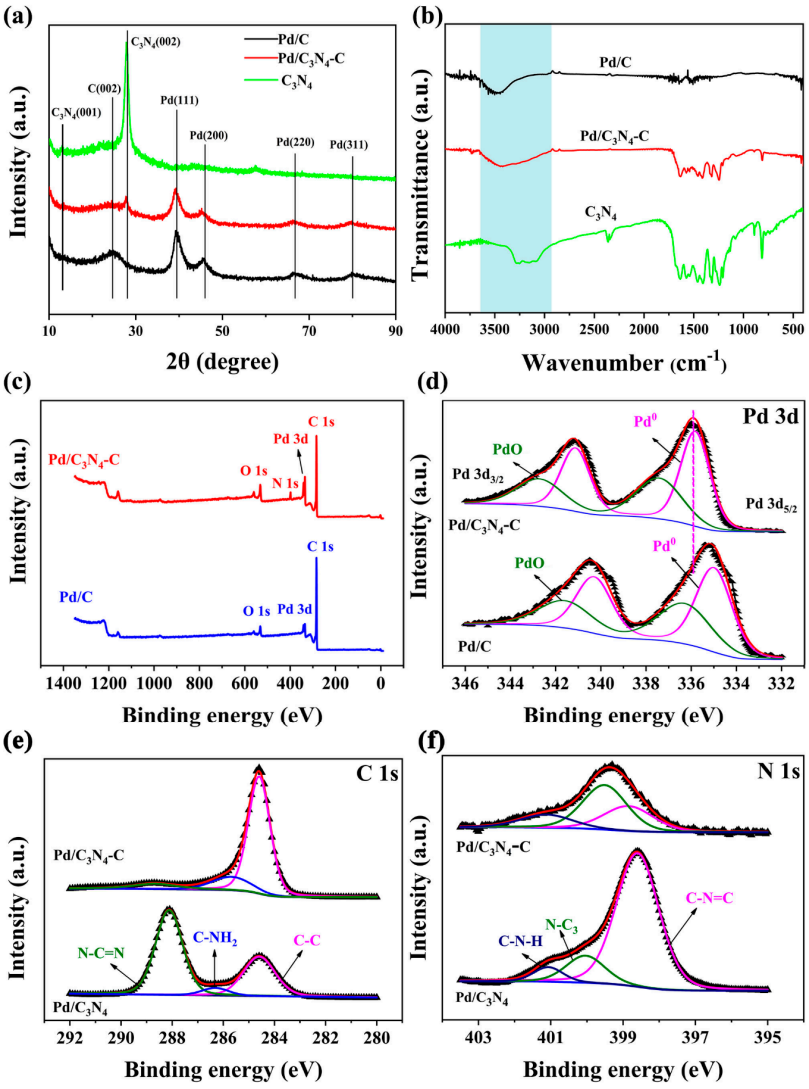

Figure 3. (**a**) XRD patterns and (**b**) FTIR spectra of Pd/C_3N_4-C, Pd/C, and C_3N_4 catalysts. (**c**) XPS full spectra of Pd/C and Pd/C_3N_4-C, (**d**–**f**) XPS spectra of Pd 3d, C 1s, and N 1s.

The vibration bands [27–30] in the region of 2900–3500 cm^{-1}, 1200–1700 cm^{-1}, and ~ 800 cm^{-1} are shown in the infrared spectra of C_3N_4 (Figure 3b). The peak at 2900–3500 cm^{-1} corresponds to the stretching vibration of the uncondensed residual of the $–NH_2$ and the –OH bond from the adsorbed water molecules. The peak at 1200–1700 cm^{-1} is attributed to the stretching vibration of the carbon–nitrogen heterocycle [C–NH–C or C–N(–C)–C]. The peak at 800 cm^{-1} is a typical triazine-absorption vibration. The three vibration bands in C_3N_4 are also preserved in Pd/C_3N_4-C.

The XPS spectra are shown in Figure 3c–f. Figure 3c reveals the coexistence of Pd, C, and N (or Pd, C) elements in the catalysts. The Pd 3D peak (Figure 3d) of Pd/C_3N_4-C positively shifted to 0.71 eV compared with Pd/C. It indicates that the synergy between C_3N_4 and carbon results in an electron-deficient state of Pd [31]. As mentioned above, the Schottky effect of C_3N_4-Pd facilitates electron migration from metal to the N-type semiconductor C_3N_4. The C 1s region (Figure 3e) can be fitted into three peaks [32–35]. The peak at 284.6 eV corresponds to the special sp^2 bond or carbon pollution in C_3N_4. The peak at 286.4 eV is attributed to the hybrid C of C–NH_2 in C_3N_4, and the C peak at 288.2 eV (Pd/C_3N_4) or 288.8 eV (Pd/C_3N_4-C) is attributed to N–C=N cyclic sp^2 hybrid C in C_3N_4. The relative proportion of different forms of carbon species can be obtained from C 1s spectra (Table 2). The N 1s region can be fitted into three peaks (Figure 3f). The peak at 398.6 eV (Pd/C_3N_4) or 398.8 eV (Pd/C_3N_4-C) corresponds to the C–N=C bond formed by the sp^2 hybrid aromatic ring N and C atom. The N peak at 400.0 eV (Pd/C_3N_4) or 399.5 eV (Pd/C_3N_4-C) is attributed to the N–C_3 bond. The N peaks at 401.1 eV (Pd/C_3N_4 or Pd/C_3N_4-C) are attributed to the residual H–N functional group derived from melamine. As shown in the N 1s spectra, the proportion of N–C_3 in Pd/C_3N_4-C (50.8 atom%) is nearly three times more than the 17.1 atom% of Pd/C_3N_4 (Table 3). As mentioned above, the XRD analysis suggests that the assembly of C_3N_4 and Vulcan carbon mainly occurs at their (002) crystal planes. The extra N–C_3 bonds mainly form between the (002) crystal plane of Vulcan carbon and the (002) plane of C_3N_4. Then the electron's transportability of C_3N_4 can be improved in the composites by the new electronic transmission path, such as some N–C_3 bonds between C_3N_4 and carbon black, and metal nanoparticles, which bridge the C_3N_4 and carbon black mentioned above.

Table 2. Percentages of carbon species from spectra of C 1s.

Electrocatalyst	C Specie	eV	Atom %
Pd/C_3N_4	C–NH_2	286.4	8.2
-	N–C=N	288.2	58.5
-	C–C	284.6	33.3
Pd/C_3N_4-C	C-NH_2	285.7	15.5
-	N–C=N	288.8	9.1
-	C–C	284.6	75.4

Table 3. Percentages of nitrogen species from spectra of N 1s.

Electrocatalyst	N Specie	eV	Atom %
Pd/C_3N_4	N–C_3	400.0	17.1
-	C–N=C	398.6	76.3
-	C–N–H	401.1	6.7
Pd/C_3N_4-C	N–C_3	399.5	50.8
-	C–N=C	398.8	31.7
-	C–N–H	401.1	17.5

2.2. Electrochemical Characterization

Cyclic voltammetry (CV) curves (Figure 4) of Pd/C, Pd/C_3N_4-C, and Pd/C_3N_4 were operated in 0.1 M NaOH solutions with and without the presence of 10 mM glucose, respectively. After the addition of glucose, an obvious oxidation current appeared at ~ 0.1 V. The glucose oxidation current at Pd/C_3N_4-C is significantly higher than that at Pd/C and Pd/C_3N_4. The current density of the glucose electrooxidation peak is used to evaluate the catalytic activity [3]. The current density of the anode peak at Pd/C_3N_4-C (31.10 mA mg^{-1}_{Pd}) is ~ 50% higher than that at Pd/C (21.15 mA mg^{-1}_{Pd}). As shown in the analysis of TEM images and XRD data, the particle size of Pd NPs in Pd/C_3N_4-C is smaller than in Pd/C. Accordingly, the electrocatalytic performance of the Pd/C_3N_4-C is better. Besides, the Schottky effect of C_3N_4-Pd [9] facilitates electron migration from metal to the N-type semiconductor C_3N_4, which benefits the electrooxidation reaction at Pd. The peak in (−0.1 ~ −0.7) V is the reduction peak of Pd(II) oxide. The glucose oxidation current at Pd/C_3N_4 is much lower than those at both Pd/C_3N_4-C and Pd/C. The lower current is due to the higher resistance of the semiconductor C_3N_4. Compared to the conductivity of the semiconductor C_3N_4 in Pd/C_3N_4, as mentioned above, the electron transportability of the C_3N_4 in the Pd/C_3N_4-C composites has been improved by adding more electronic transmission paths such as N–C_3 bonds bridging carbon black and C_3N_4, and metal nanoparticles bridging the C_3N_4 and carbon black.

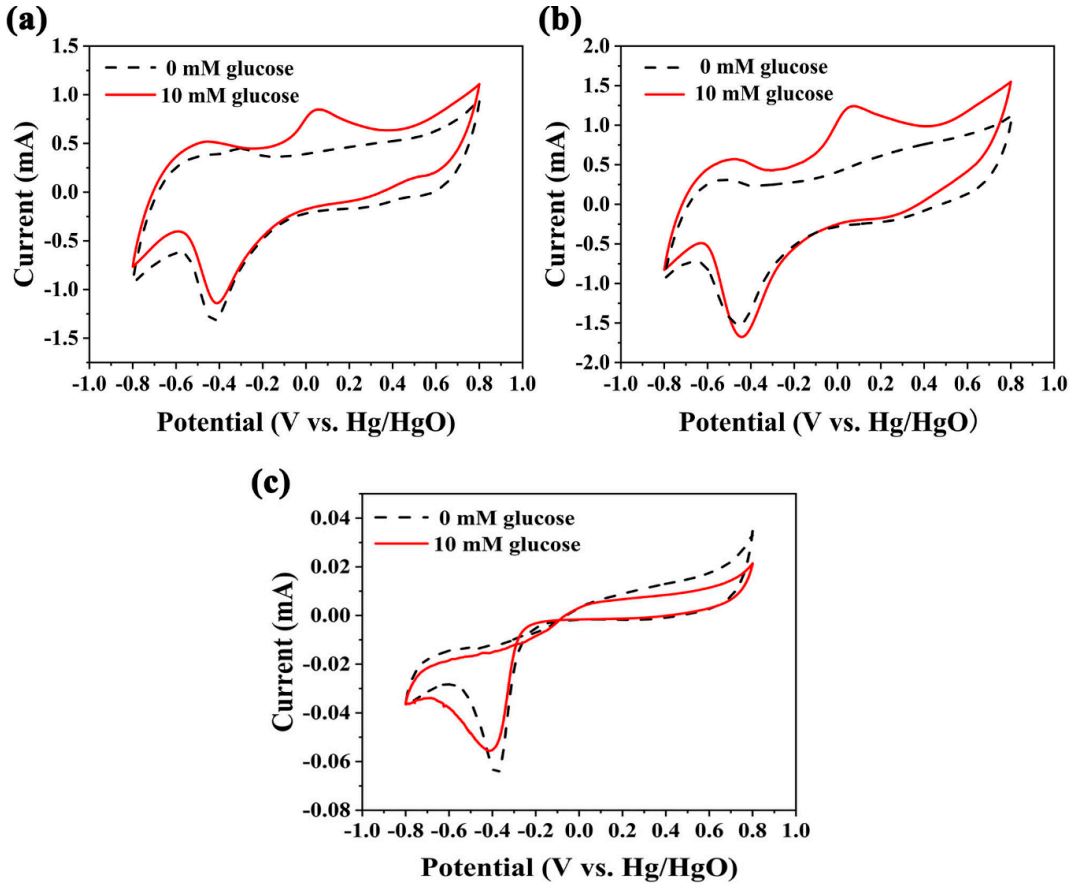

Figure 4. Cyclic voltammetries (CVs) at of (**a**) Pd/C, (**b**) Pd/C_3N_4-C, and (**c**) Pd/C_3N_4, 0.1 M NaOH solution, and 50 mV s^{-1}.

2.3. Glucose Sensing

Figure 5a is the CV curves of Pd/C_3N_4-C at different scan rates (50 ~ 500 mV s^{-1}). Ten mM glucose in a 0.1 M NaOH solution was used as the sample. 0.1 M NaOH has been widely used as the media for the evaluation of the electrocatalytic activity of Pd NPs for GOR [12,36–38]. It can be seen that as

the scan rate increases, the current also increases (Figure 5a). However, when the scan rate is higher than 50 mV s^{-1}, the peak is not obvious. So 50 mV s^{-1} was chosen as the scan rate for glucose sensing. The fitting curve (Figure 5b) indicates the relationship between the scanning speed and the peak current. The anode peak current has a linear relationship with the square root of the scanning rate ($y = 0.138\ x - 0.295$, $R^2 = 0.996$), which reveals that the glucose oxidation is controlled by the diffusion during the voltammetric measurements.

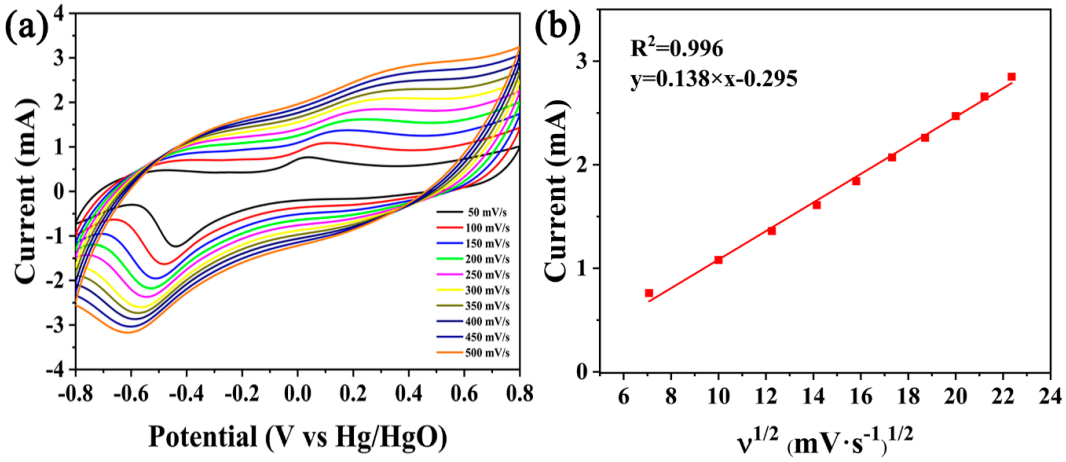

Figure 5. (**a**) CVs of the glucose electrooxidation reaction (GOR) at Pd/C_3N_4-C and (**b**) the corresponding plots of the anode peak currents vs. the square root of the scan rates in a 10 mM glucose +0.1 M NaOH solution.

The linear scanning voltammetry (LSV) curves (Figure 6a) of Pd/C_3N_4-C under different glucose concentrations (1–10 mM) and the corresponding calibration curve (Figure 6b) were obtained in alkaline solutions, and the regression equation is I (mA) = 0.0344·c (mM) + 0.0216 (R^2 = 0.992). Figure 6c displays the amperometric response to glucose at Pd/C_3N_4-C, and Pd/C at 0.5 V. Pd/C_3N_4-C has a rapid response (less than 7 s) in glucose sensing, implying sensitive and fast responses to GOR. Amperometric responses of Pd/C_3N_4-C are more sensitive than Pd/C. The calibration curve (Figure 6d) shows that the glucose oxidation current increased linearly in the concentration range of 0.001 to 10 mM and 11 to 20 mM, respectively. At glucose concentration of 0.001 to 10 mM, the regression equation of Pd/C_3N_4-C is I (mA) = 0.00877·C (mM) + 0.00763 (R^2 = 0.993) and the regression equation of Pd/C is I (mA) = 0.00263·C (mM) + 0.00744 (R^2 = 0.996). At higher concentrations with a range such as 11–20 mM, the regression equation is I (mA) = 0.00498·C (mM) + 0.0389 (R^2 = 0.997) and the regression equation of Pd/C is I (mA) = 0.00179·C (mM) + 0.0156 (R^2 = 0.998). The sensitivity for Pd/C_3N_4-C and Pd/C in the concentration range of 0.001 to 10 mM is calculated to be 219 and 65.7 μA mM^{-1} $mg^{-1}{}_{Pd}$, respectively. The sensitivity of Pd/C_3N_4-C is ~ 3.3 times of Pd/C. The limits of detection (LOD) for Pd/C_3N_4-C and Pd/C (S/N = 3) were calculated to be 0.55 μM and 3.1 μM, respectively. (LOD = 3σ/S [39], where σ is the standard deviation of 5 blanks, and S is the slope of the linear regression equation. S/N = 3). The relative standard deviation (RSD) is 4.5% (five repeated measurements). Figure 6e is an enlarged view of the current response calibration curve at 0.1–1 mM. The sensitivity of Pd/C_3N_4-C in the range of 0.001–1 mM is ~ 10 times greater than Pd/C. The calibration curves of both the voltammetric and the amperometric measurements confirm the sensitive and linear response of Pd/C_3N_4-C to the glucose in alkaline media. The responses of KCl (0.1 mM), NaCl(0.1 mM), lactose(0.1 mM), ascorbic acid (AA, 20 μM), and uric acid (UA,120 μM) were also recorded at 0.5 V (Figure 6f). The responses of 1 mM glucose were used as contrasts. Pd/C_3N_4-C exhibits conspicuous resistance to these interfering substances during the GOR.

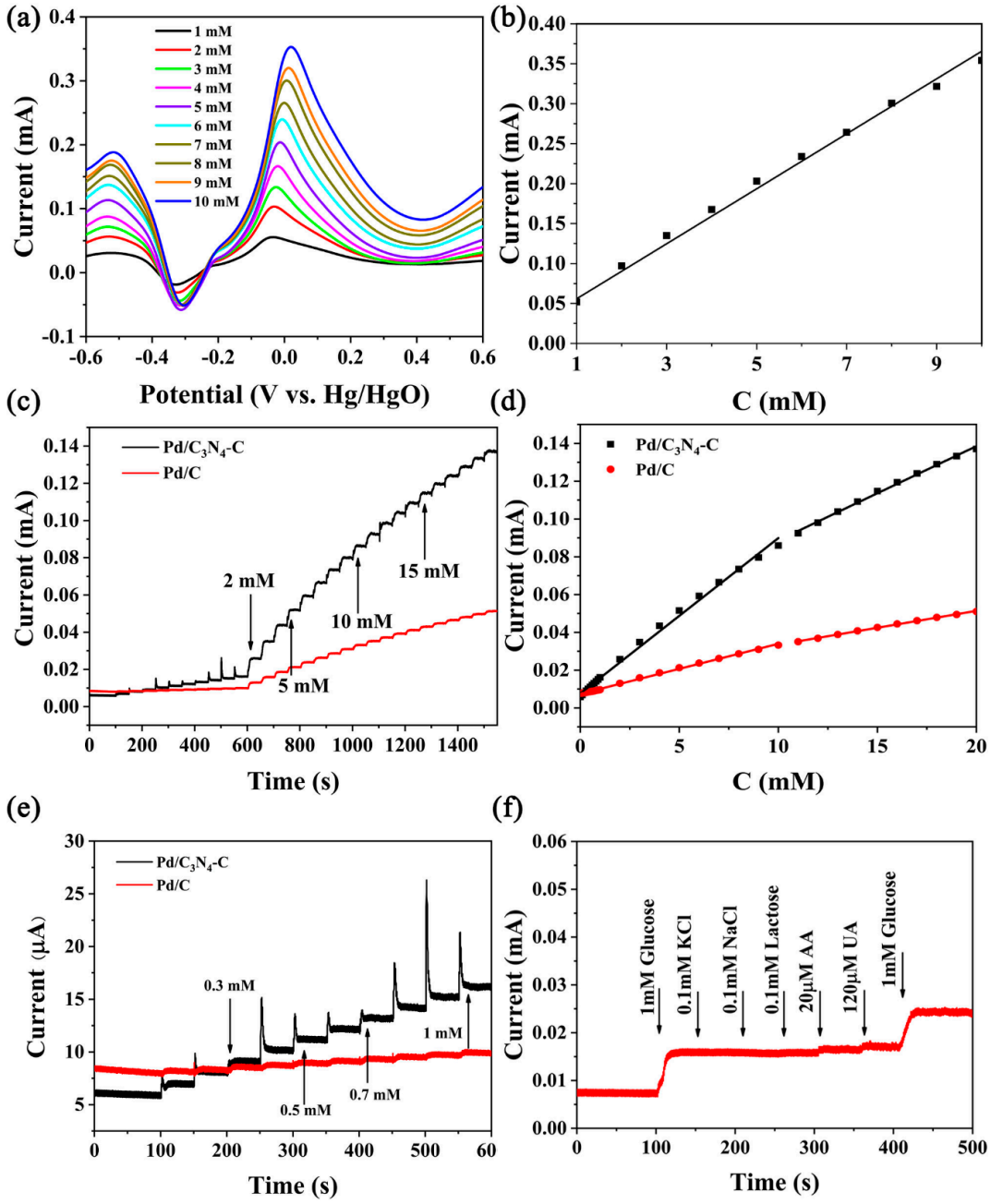

Figure 6. (**a**) The linear scanning voltammetry (LSV) curves of Pd/C_3N_4-C in the presence of glucose in 0.1 M NaOH. The scan rate of 50 mV s^{-1}. (**b**) The calibration curve of glucose sensing at Pd/C_3N_4-C corresponding to the LSV curves. (**c**) The amperometric responses of Pd/C_3N_4-C and Pd/C to glucose. 0.5 V vs. Hg/HgO. (**d**) The calibration curves obtained from the amperometric curves. (**e**) The amperometric response of 0.1–1 mM glucose at Pd/C_3N_4-C and Pd/C. (**f**) The current response of Pd/C_3N_4-C to interfering substances compared with glucose.

The glucose concentration after the electrocatalytic oxidation was determined in order to obtain the percentage of degradation. Figure 7 shows the LSV curves at Pd/C_3N_4-C before and after 200 CV cycles. According to the glucose concentrations obtained from the linear equation in Figure 6b, the percentage of degradation is 32% after 200 CV cycles.

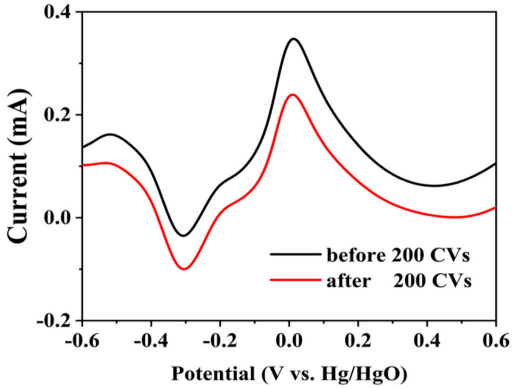

Figure 7. LSVs at Pd/C_3N_4-C before and after 200 CVs. Ten mM glucose, and 0.1 M NaOH. 50 mV s^{-1}.

3. Materials and Methods

3.1. Materials and Instruments

Nafion (5 wt%, Dupont, Delaware, DE, USA) and carbon black (XC-72R, Cabot Corp., Waltham, MA, USA) were used as obtained. All other chemicals were of analytical grade and used as received. Trip-distilled water was used during the whole experimental process.

FTIR (Nicolet iS10 spectrometer, Thermo Fisher Scientific, Waltham, MA, USA), XPS (XSAM-800 spectrometer, Kratos Analytical Ltd., Manchester, UK), XRD (D8 Advance instrument, Bruker, Karlsruhe, Germany, Cu Kα radiation at λ = 0.15406 nm), SEM (SU-70 microscope, Hitachi, Tokyo, Japan), and TEM (JEM-1011, JEOL, Beijing, China, acceleration voltage 200 kV) were used for the physical characterization of the electrocatalysts.

3.2. Preparation of C_3N_4 and Pd/C_3N_4-C

The preparation of C_3N_4 and Pd/C_3N_4-C is schematically illustrated in Figure 8. The C_3N_4 was prepared by the pyrolysis of melamine at 550 °C in a tube furnace for 4 h. The obtained C_3N_4 was ground into powders after natural cooling. The powders were filtered through a 500-mesh sieve. Sixteen mg C_3N_4 and 24 mg carbon black were added to 25 mL of triple-distilled water and dispersed ultrasonically. Then, a certain amount of $PdCl_2$ solution (10 mg Pd) was added to the suspension and stirred. After the pH of the mixture was adjusted to 10, a 10 mL 5 wt % $NaBH_4$ solution was added. The reaction mixture was stirred for 6 h and left to stand overnight. The obtained Pd/C_3N_4-C products were filtered and washed. Then, the catalysts were dried in a vacuum oven (60 °C, 10 h). Pd/C (or Pd/C_3N_4) was synthesized under identical conditions except for the replacement of C_3N_4-C with 40 mg of C (or C_3N_4). The metal loading was 20 wt % in the as-prepared catalyst.

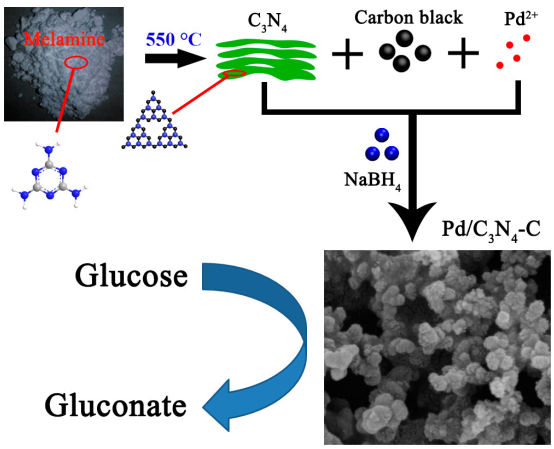

Figure 8. Schematic depiction of the formation of porous Pd/C_3N_4-C.

3.3. Electrochemical Experiments of Glucose Sensors and GOR Analysis

Electrochemical tests were conducted in a standard three-electrode system using the CHI660E electrochemical workstation, including a carbon rod as the counter electrode, a Hg/HgO (saturated 1 M NaOH) electrode as the reference electrode, and a modified 3-mm-diameter GCE as the working electrode. All the potentials are quoted with respect to Hg/HgO reference in this paper.

To fabricate the modified GCE working electrode, the GCE should be polished by 0.05 μm Al_2O_3 nanoparticles before use. The ink of catalyst should be prepared by dispersing 10 mg of the catalyst in a mixture of 0.5 mL ethanol and 0.5 mL triple-distilled water ultrasonically. Twenty μL (4 μL × 5 aliquots) of the ink should be dropped onto the GCE surface. This drop of ink should be dried, then another drop should be added. The deposited ink should be finally covered with 4 μL of a Nafion solution. The Nafion solution should also be dried at room temperature. The as-prepared modified GCE was used as the working electrode. The catalysts in 10 μL of ink were enough to cover the whole surface of the 3-mm diameter GCE after the ink dried [40]. A higher amount of catalysts is beneficial to improve the durability or long-term stability of the modified GCE. For example, in our previous work, we dropped 34 μL of ink onto a GCE [41] for the oxygen-reduction reaction. The as-prepared electrode kept a stable electrocatalytic current density during a long-term (84 h) measurement. In this work, a compromised amount (20 μL of ink) of catalysts was used to prepare the working electrodes.

Voltammetric measurements were obtained in the mixture solution of NaOH and glucose. The electrolyte solutions were bubbled with nitrogen for more than 20 min before use. The bubbled solutions were used under a nitrogen atmosphere during the electrochemical measurements. The sensitivity and interference of Pd/C_3N_4-C were recorded in a stirred glucose/NaOH solution at a fixed potential of 0.5 V.

4. Conclusions

Coral-like porous Pd/C_3N_4-C electrocatalysts were synthesized by a simple room-temperature reduction method. The introduction of C_3N_4 significantly decreased the Pd nanoparticle's size and increased its dispersion, which is beneficial for the improvement of the electrocatalytic activity of Pd for GOR. Pd/C_3N_4-C also exhibits a highly sensitive, fast, selective, and linear amperometric response to glucose, which makes this electrocatalyst a good candidate for nonenzymatic-glucose sensors. The N–C_3 bonds between C_3N_4 and carbon improved the conductivity of the semiconductor C_3N_4 in the composites, which facilitates the application of C_3N_4 in the field of electrocatalysts.

Author Contributions: Conceptualization, G.D. and W.L.; validation, Y.G. and H.Z.; formal analysis, C.L.; investigation, G.D. and Q.L.; resources, C.L.; data curation, G.D.; writing—original draft preparation, G.D.; writing—review and editing, Q.L.; supervision, W.L.; project administration, H.J.; funding acquisition, H.J. All authors have read and agreed to the published version of the manuscript.

Funding: This work was funded by the Key Technology Research and Development Program of Shandong Province (2019GSF111014), the Natural Science Foundation of Shandong Province (ZR2016BM31), and the Introduction and Cultivation Plan of Young Innovative Talents in Colleges and Universities of Shandong Province.

Conflicts of Interest: The authors declare no conflict of interest.

References

1. Heller, A.; Feldman, B. Electrochemical glucose sensors and their applications in diabetes management. *Chem. Rev.* **2008**, *108*, 2482–2505. [CrossRef] [PubMed]
2. Adzic, R.R.; Hsiao, M.W.; Yeager, E.B. Electrochemical oxidation of glucose on single crystal gold surfaces. *J. Electroanal. Chem. Interfacial Electrochem.* **1989**, *260*, 475–485. [CrossRef]
3. Song, S.; Wang, K.; Yan, L.; Brouzgou, A.; Zhang, Y.; Wang, Y.; Tsiakaras, P. Ceria promoted Pd/C catalysts for glucose electrooxidation in alkaline media. *Appl. Catal. B Environ.* **2015**, *176–177*, 233–239. [CrossRef]
4. Brouzgou, A.; Tsiakaras, P. Electrocatalysts for glucose electrooxidation reaction: A Review. *Top. Catal.* **2015**, *58*, 1311–1327. [CrossRef]

5. Wang, Q.; Cui, X.; Chen, J.; Zheng, X.; Liu, C.; Xue, T.; Wang, H.; Jin, Z.; Qiao, L.; Zheng, W. Well-dispersed palladium nanoparticles on graphene oxide as a non-enzymatic glucose sensor. *RSC Adv.* **2012**, *2*, 6245–6249. [CrossRef]
6. Rafaïdeen, T.; Baranton, S.; Coutanceau, C. Highly efficient and selective electrooxidation of glucose and xylose in alkaline medium at carbon supported alloyed PdAu nanocatalysts. *Appl. Catal. B Environ.* **2019**, *243*, 641–656. [CrossRef]
7. Wu, W.; Miao, F.; Tao, B.; Zang, Y.; Zhu, L.; Shi, C.; Chu, P.K. Hybrid ZnO-graphene electrode with palladium nanoparticles on Ni foam and application to self-powered nonenzymatic glucose sensing. *RSC Adv.* **2019**, *9*, 12134–12145. [CrossRef]
8. El-Ads, E.H.; Galal, A.; Atta, N.F. The effect of A-site doping in a strontium palladium perovskite and its applications for non-enzymatic glucose sensing. *RSC Adv.* **2016**, *6*, 16183–16196. [CrossRef]
9. Ni, Z.; Dong, F.; Huang, H.; Zhang, Y. New insights into how Pd nanoparticles influence the photocatalytic oxidation and reduction ability of g-C_3N_4 nanosheets. *Catal. Sci. Technol.* **2016**, *6*, 6448–6458. [CrossRef]
10. Wu, Y.S.; Wu, Z.W.; Lee, C.L. Concave Pd core/island Pt shell nanoparticles: Synthesis and their promising activities toward neutral glucose oxidation. *Sens. Actuators B Chem.* **2019**, *281*, 1–7. [CrossRef]
11. Ma, J.; Chen, Y.; Chen, L.; Wang, L. Ternary Pd–Ni–P nanoparticle-based nonenzymatic glucose sensor with greatly enhanced sensitivity achieved through active-site engineering. *Nano Res.* **2017**, *10*, 2712–2720. [CrossRef]
12. Ye, J.S.; Chen, C.W.; Lee, C.L. Pd nanocube as non-enzymatic glucose sensor. *Sens. Actuators B Chem.* **2015**, *208*, 569–574. [CrossRef]
13. Ponnusamy, R.; Chakraborty, B.; Rout, C.S. Pd-Doped WO_3 Nanostructures as Potential Glucose Sensor with Insight from Electronic Structure Simulations. *J. Phys. Chem. B* **2018**, *122*, 2737–2746. [CrossRef] [PubMed]
14. Yang, C.; Cui, X.; Wang, K.; Cao, Y.; Wang, C.; Hu, X. A non-enzymatic glucose sensor based on Pd-Fe/Ti nanocomposites. *Int. J. Electrochem. Sci.* **2017**, *12*, 5492–5502. [CrossRef]
15. Dhara, K.; Thiagarajan, R.; Nair, B.G.; Thekkedath, G.S.B. Highly sensitive and wide-range nonenzymatic disposable glucose sensor based on a screen printed carbon electrode modified with reduced graphene oxide and Pd-CuO nanoparticles. *Microchim. Acta* **2015**, *182*, 2183–2192. [CrossRef]
16. Li, Y.; Niu, X.; Tang, J.; Lan, M.; Zhao, H. A comparative study of nonenzymatic electrochemical glucose sensors based on Pt-Pd nanotube and nanowire arrays. *Electrochim. Acta* **2014**, *130*, 1–8. [CrossRef]
17. Shen, C.; Su, J.; Li, X.; Luo, J.; Yang, M. Electrochemical sensing platform based on Pd-Au bimetallic cluster for non-enzymatic detection of glucose. *Sens. Actuators B Chem.* **2015**, *209*, 695–700. [CrossRef]
18. Liu, Q.; Tang, Y.; Yang, X.; Wei, M.; Zhang, M. An ultra-low detection limit glucose sensor based on reduced graphene oxide-concave tetrahedral Pd NCs@CuO composite. *J. Electrochem. Soc.* **2019**, *166*, B381–B387. [CrossRef]
19. Vilé, G.; Albani, D.; Nachtegaal, M.; Chen, Z.; Dontsova, D.; Antonietti, M.; López, N.; Pérez-Ramírez, J. A stable single-site palladium catalyst for hydrogenations. *Angew. Chemie Int. Ed.* **2015**, *54*, 11265–11269. [CrossRef]
20. Ye, L.; Liu, J.; Jiang, Z.; Peng, T.; Zan, L. Facets coupling of BiOBr-g-C_3N_4 composite photocatalyst for enhanced visible-light-driven photocatalytic activity. *Appl. Catal. B Environ.* **2013**, *142–143*, 1–7. [CrossRef]
21. Lv, M.; Li, W.; Liu, H.; Wen, W.; Dong, G.; Liu, J.; Peng, K. Enhancement of the formic acid electrooxidation activity of palladium using graphene/carbon black binary carbon supports. *Chin. J. Catal.* **2017**, *38*, 939–947. [CrossRef]
22. Radmilovic, V.; Gasteiger, H.A.; Ross, P.N. Structure and chemical composition of a supported Pt-Ru electrocatalyst for methanol oxidation. *J. Catal.* **1995**, *154*, 98–106. [CrossRef]
23. Holzwarth, U.; Gibson, N. The Scherrer equation versus the "Debye-Scherrer equation". *Nat. Nanotechnol.* **2011**, *6*, 534. [CrossRef] [PubMed]
24. Uruş, S.; Çaylar, M.; Karteri, İ. Synthesis of graphene supported bis(diphenylphosphinomethyl)amino ligands and their Pd(II) and Pt(II) complexes: Highly efficient and recoverable nano-catalysts on vitamin K_3 production. *Chem. Eng. J.* **2016**, *306*, 961–972. [CrossRef]
25. Wang, C.-H.; Yang, C.-H.; Chang, J.-K. High-selectivity electrochemical non-enzymatic sensors based on graphene/Pd nanocomposites functionalized with designated ionic liquids. *Biosens. Bioelectron.* **2017**, *89*, 483–488. [CrossRef]

26. Elango, G.; Roopan, S.M.; Al-Dhabi, N.A.; Arasu, M.V.; Dhamodaran, K.I.; Elumalai, K. Coir mediated instant synthesis of Ni-Pd nanoparticles and its significance over larvicidal, pesticidal and ovicidal activities. *J. Mol. Liq.* **2016**, *223*, 1249–1255. [CrossRef]
27. Yu, X.; Fan, T.; Chen, W.; Chen, Z.; Dong, Y.; Fan, H.; Fang, W.; Yi, X. Self-hybridized coralloid graphitic carbon nitride deriving from deep eutectic solvent as effective visible light photocatalysts. *Carbon N. Y.* **2019**, *144*, 649–658. [CrossRef]
28. Zhou, C.; Lai, C.; Huang, D.; Zeng, G.; Zhang, C.; Cheng, M.; Hu, L.; Wan, J.; Xiong, W.; Wen, M.; et al. Highly porous carbon nitride by supramolecular preassembly of monomers for photocatalytic removal of sulfamethazine under visible light driven. *Appl. Catal. B Environ.* **2018**, *220*, 202–210. [CrossRef]
29. Li, Y.; Ho, W.; Lv, K.; Zhu, B.; Lee, S.C. Carbon vacancy-induced enhancement of the visible light-driven photocatalytic oxidation of NO over g-C_3N_4 nanosheets. *Appl. Surf. Sci.* **2018**, *430*, 380–389. [CrossRef]
30. Yan, S.C.; Li, Z.S.; Zou, Z.G. Photodegradation performance of g-C_3N_4 fabricated by directly heating melamine. *Langmuir* **2009**, *25*, 10397–10401. [CrossRef]
31. Yi, H.; Xia, Y.; Yan, H.; Lu, J. Coating Pd/Al_2O_3 catalysts with FeO_x enhances both activity and selectivity in 1,3-butadiene hydrogenation. *Chin. J. Catal.* **2017**, *38*, 1581–1587. [CrossRef]
32. Darabdhara, G.; Bordoloi, J.; Manna, P.; Das, M.R. Biocompatible bimetallic Au-Ni doped graphitic carbon nitride sheets: A novel peroxidase-mimicking artificial enzyme for rapid and highly sensitive colorimetric detection of glucose. *Sens. Actuators B Chem.* **2019**, *285*, 277–290. [CrossRef]
33. Yang, X.; Tian, L.; Zhao, X.; Tang, H.; Liu, Q.; Li, G. Interfacial optimization of g-C_3N_4-based Z-scheme heterojunction toward synergistic enhancement of solar-driven photocatalytic oxygen evolution. *Appl. Catal. B Environ.* **2019**, *244*, 240–249. [CrossRef]
34. Yang, Y.; Zhang, C.; Huang, D.; Zeng, G.; Huang, J.; Lai, C.; Zhou, C.; Wang, W.; Guo, H.; Xue, W.; et al. Boron nitride quantum dots decorated ultrathin porous g-C_3N_4: Intensified exciton dissociation and charge transfer for promoting visible-light-driven molecular oxygen activation. *Appl. Catal. B Environ.* **2019**, *245*, 87–99. [CrossRef]
35. Zhang, W.; Li, X.; Xu, X.; He, Y.; Qiu, F.; Pan, J.; Niu, X. Pd nanoparticle-decorated graphitic C_3N_4 nanosheets with bifunctional peroxidase mimicking and ON-OFF fluorescence enable naked-eye and fluorescent dual-readout sensing of glucose. *J. Mater. Chem. B* **2019**, *7*, 233–239. [CrossRef]
36. Chen, X.M.; Lin, Z.J.; Chen, D.J.; Jia, T.T.; Cai, Z.M.; Wang, X.R.; Chen, X.; Chen, G.N.; Oyama, M. Nonenzymatic amperometric sensing of glucose by using palladium nanoparticles supported on functional carbon nanotubes. *Biosens. Bioelectron.* **2010**, *25*, 1803–1808. [CrossRef]
37. Singh, B.; Bhardwaj, N.; Jain, V.K.; Bhatia, V. Palladium nanoparticles decorated electrostatically functionalized MWCNTs as a non enzymatic glucose sensor. *Sens. Actuators Phys.* **2014**, *220*, 126–133. [CrossRef]
38. Chen, X.; Li, G.; Zhang, G.; Hou, K.; Pan, H.; Du, M. Self-assembly of palladium nanoparticles on functional TiO_2 nanotubes for a nonenzymatic glucose sensor. *Mater. Sci. Eng. C* **2016**, *62*, 323–328.
39. Mao, X.; Yang, X.; Rutledge, G.C.; Alan Hatton, T. Ultra-wide-range electrochemical sensing using continuous electrospun carbon nanofibers with high densities of states. *ACS Appl. Mater. Interfaces* **2014**, *6*, 3394–3405. [CrossRef]
40. Wen, W.; Li, C.; Li, W.; Tian, Y. Carbon-supported Pd-Cr electrocatalysts for the electrooxidation offormic acid that demonstrate high activity and stability. *Electrochim. Acta* **2013**, *109*, 201–206. [CrossRef]
41. Li, W.; Fan, F.R.F.; Bard, A.J. The application of scanning electrochemical microscopy to the discovery of Pd-welectrocatalysts for the oxygen reduction reaction that demonstrate high activity, stability, and methanol tolerance. *J. Solid State Electrochem.* **2012**, *16*, 2563–2568. [CrossRef]